


Modeling of the photocurrent induced by inverse spin Hall effect under local circularly polarized photoexcitation

Kuen Wai Tang , Bob Minyu Wang, Henry Clark Travaglini, and Dong Yu *

Department of Physics, University of California–Davis, One Shields Avenue, Davis, California 95616, USA



(Received 9 September 2021; revised 26 October 2021; accepted 27 October 2021; published 8 November 2021)

The inverse spin Hall effect (ISHE) has been recently demonstrated through the photoinduced inverse spin Hall effect (PISHE), where a focused laser normal to the device plane generates photocurrent that depends on the helicity of the photoexcitation. Here, we have employed a finite element method to rigorously simulate the helicity-dependent photocurrent (HDPC) under local helical photoexcitation, taking into account the complications of minority carriers, metal contact junctions, and spin relaxation. We found that the ISHE-induced electromotive force is inversely proportional to the doping level of the material, caused by the diffusion and drift current balance. Furthermore, the HDPC near the metal contact can either increase or decrease, because of the competing mechanisms of fast carrier recombination and spin relaxation at the contact. These simulation results provide insightful visualization of charge, spin, electric field, and current density distributions and deeper understanding of photoinduced ISHE.

DOI: [10.1103/PhysRevB.104.205413](https://doi.org/10.1103/PhysRevB.104.205413)

I. INTRODUCTION

The inverse spin Hall effect (ISHE) refers to the generation of a charge current transverse to a spin current and is the reverse process of the spin Hall effect (SHE). Both SHE and ISHE are created by spin-orbit interaction (SOI) [1]. ISHE has been observed through local circularly polarized photoexcitation in $\text{Al}_x\text{Ga}_{1-x}\text{N}/\text{GaN}$ [2], InN [3], and more recently in topological insulators (TIs) [4–6]. Rashba spin splitting [7,8] and spin-momentum locking at the surfaces of TIs [9] can also generate circular photogalvanic effects (CPGE), but only at oblique incidence, since in-plane electron spin is needed in these cases. In contrast, photoinduced ISHE (PISHE) is usually performed at normal incidence to eliminate these complications and is often referred to as anomalous PISHE.

The typical experimental setup to measure PISHE is sketched in Fig. 1, where the circular polarization can be reversed from left to right by using a rotating quarter waveplate (QWP). This experimental method can be regarded as an extension of scanning photocurrent microscopy (SPCM), which has been used to extract electronic band structures and charge carrier diffusion lengths in optoelectronic materials [10,11]. Adding the circular polarization dependence into this powerful technique further extends its capability to understand and manipulate spin and/or charge transport in semiconductor devices [5,12–14].

In prior work [2,4,6], PISHE has been understood by modeling a nonelectrostatic electromotive force (EMF) transverse to the radial spin diffusion current from the local spin injection. Nevertheless, several important questions have not been addressed: (1) Both majority and minority charge carriers can contribute to electric current [10,11] but previous

work only considers the majority charge carriers. (2) A strong electric field often develops in the depletion region near the semiconductor and metal junction, whose impact on HDPC is unclear. (3) How the spin relaxation process influences the HDPC distribution is unclear. In this work, we perform comprehensive modeling to address the above questions.

II. MODEL AND METHOD

Our model is based on the steady-state continuity equations for spin-polarized electrons and holes. A focused circularly polarized CW laser locally generates spin polarized electrons and holes, which undergo recombination and spin-relaxation processes. These photogenerated electrons and holes diffuse and drift, driven by the concentration gradient and electric field. Because these carriers carry spins, their transport is also influenced by ISHE. To simplify the problem, we assume that the hole spin relaxation is much faster than that of electrons and hence ignore hole spin [15]. The continuity equation for electrons is

$$\frac{dn_\lambda}{dt} = G_\lambda - b(n_\lambda p - n_i^2/2) - \frac{n_\lambda - n_{-\lambda}}{2\tau_s} - \nabla \cdot \vec{J}_{n_\lambda}. \quad (1)$$

Here, $\lambda = 1$ corresponds to spin up (\uparrow), $\lambda = -1$ corresponds to spin down (\downarrow), and τ_s is the spin relaxation time. G is the photogeneration rate and n_i is the intrinsic carrier concentration. We assume nonequilibrium charge carriers recombine through the Shockley-Read-Hall process at a rate b . The left circularly polarized (LCP) photoexcitation generates \uparrow electrons only ($G = G_\uparrow$ and $G_\downarrow = 0$), and vice versa for right circular polarization (RCP). As most PISHE experiments are performed under steady-state situations, we assume all physical quantities in our model are time independent and the time derivative on the left of the above equation is hence zero. The number current density of spin polarized electrons

*yu@physics.ucdavis.edu

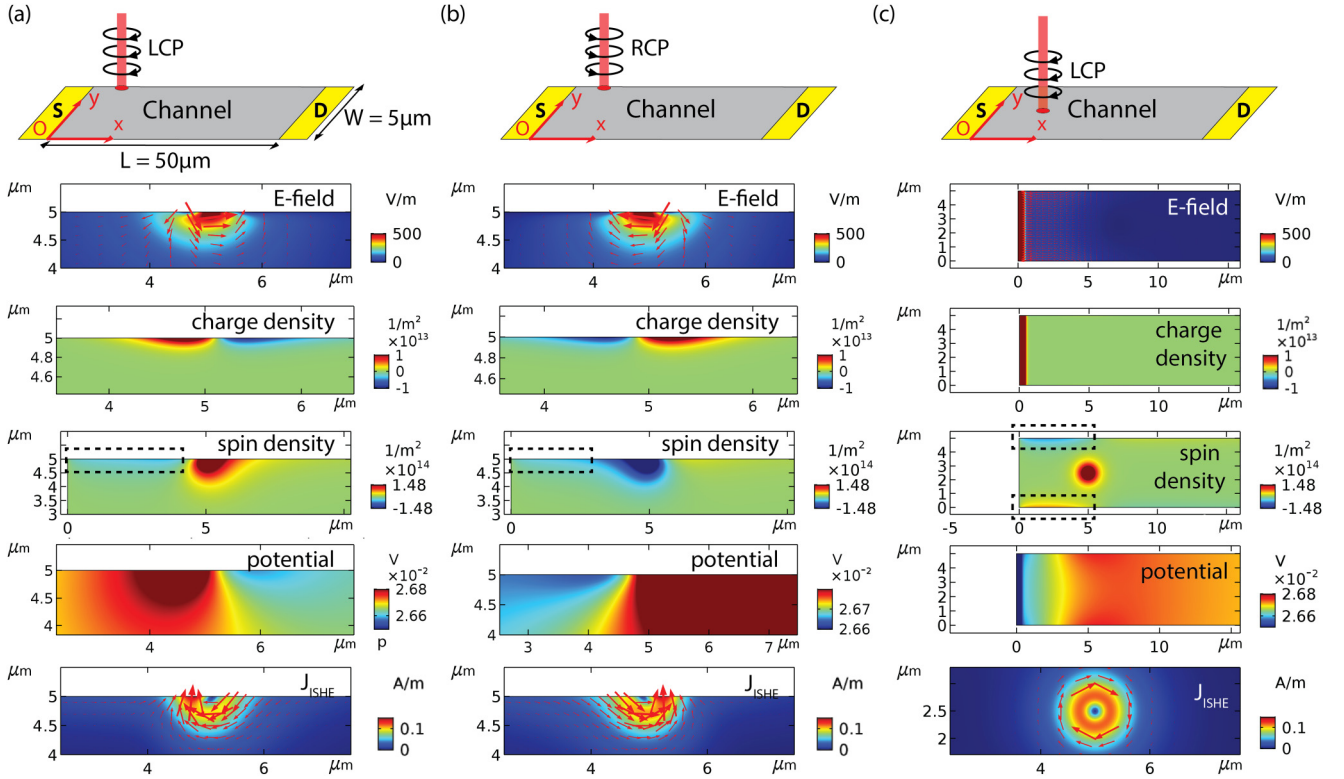


FIG. 1. The simulated distributions of electric field, charge density, spin density, electric potential, and ISHE current density, near the local photoexcitation. The origin is chosen to be at the bottom left corner of the device channel as shown. The laser is centered at $x, y = (5, 5) \mu\text{m}$ in panels (a) and (b), and $(5, 2.5) \mu\text{m}$ in panel (c). S and D indicate the source and drain contacts, respectively. The laser is LCP in panels (a) and (c) and RCP in panel (b). Dashed boxes highlight spin accumulation near the edge. Red arrows indicate the vector directions

is composed of drift, diffusion, and ISHE components as

$$\vec{J}_{n_\lambda} = -\mu_n n_\lambda \vec{E} - D_n \nabla n_\lambda + \vec{J}_{n_\lambda}^{\text{ISHE}}, \quad (2)$$

where we assume electron diffusion coefficient (D_n) and mobility (μ_n) are independent of spin. The number current density multiplying electron charge e gives the current density. The last term is the ISHE induced current, which is given by

$$\vec{J}_{n_\lambda}^{\text{ISHE}} = \lambda \gamma (\mu_n n_\lambda \vec{E} + D_n \nabla n_\lambda) \times \hat{z}. \quad (3)$$

Here, γ parameterizes the SOI strength and \hat{z} is the normal vector to the surface. The chirality of ISHE is reflected by a sign flip (λ) when spin is reversed. The trajectories of \uparrow and \downarrow electrons are bent by SOI into opposite directions, perpendicular to the sum of diffusion and drift currents. Note that previous work [2,4,6] did not consider the drift term in Eq. (3). Our simulation results show that though ignoring the drift term does not have much impact on the simulated overall HPDC, it creates false spin and charge accumulation near the corners of the depletion region (see Appendix D). Therefore, we keep the drift term in our simulations below. The complete set of equations used in the simulation are shown in Appendix A.

The device to be considered is a two-dimensional (2D) rectangle in the xy plane, such that carriers are constrained in plane, while the spins are along the z axis by a focused laser normal to the device plane, as shown in Fig. 1. This configuration is chosen to represent typical experimental conditions [6,16]. The boundary conditions are (1) the electric potential is zero at contacts and (2) charge cannot flow out

of the edges. An electron barrier with a height of Φ_B is considered between the metal contact and the semiconductor. Importantly, we also assume that the carrier recombination and spin relaxation are infinitely fast at the metal contacts, such that spin and photogenerated carrier densities both vanish at the contacts. We then carry out the numerical simulation by a finite element method using COMSOL MULTIPHYSICS. The temperature is set to 300 K and the bias voltage to 0 V for all simulations. Typical physical parameters used in the simulation are listed in Table I and more details are shown in Appendix B.

III. SIMULATION RESULTS AND DISCUSSION

A. Distributions of field, charge, and spin

The simulation allows us to visualize the distributions of electric field, spin and charge densities, potential, and ISHE current. When a LCP laser is focused at the edge [Figs. 1(a) and 1(b)], an electric field develops and curls around the injection point (shown as red arrows). The electric field is much weaker if $\gamma = 0$ [Fig. S1(c)], indicating the field is generated by ISHE. The radial spin diffusion from the center of the Gaussian beam leads to a transverse charge current. Accumulation of opposite charges at the edge forms an electric dipole as shown in Fig. 1. This dipole behaves as a local EMF and generates HDPC. However, if the laser is not close to the edge, ISHE only produces a circular transverse charge current without generating charge accumulation or HDPC [Fig. 1(c)]. This picture is consistent with a recent work [6]. The charge

TABLE I. Typical simulation parameters. Channel length and width, laser spot size, donor and acceptor concentrations, Schottky barrier height, SOI strength, and spin lifetime are varied and specified in the corresponding sections.

Symbol	Physical meaning	Value
P_{abs}	Absorbed laser power	$2 \mu\text{W}$
$h\nu$	Laser energy	2.33 eV
σ	Laser spot size	$0.2 \mu\text{m}$
L	Channel length	$50 \mu\text{m}$
W	Channel width	$5 \mu\text{m}$
N_d	Donor concentration	10^{16} m^{-2}
N_a	Acceptor concentration	0
$q\Phi_B$	Schottky barrier height	0.03 eV
γ	SOI strength	0.5
E_g	Band gap	0.3 eV
τ_n	Electron lifetime	100 ns
τ_p	Hole lifetime	100 ns
τ_s	Spin relaxation lifetime	0.1 ns
μ_n	Electron mobility	$10^3 \text{ cm}^2 \text{ V}^{-1} \text{ s}^{-1}$
μ_p	Hole mobility	$10^3 \text{ cm}^2 \text{ V}^{-1} \text{ s}^{-1}$
m_e	Effective mass of electron	$0.12 m_0$
m_h	Effective mass of hole	$0.24 m_0$
ϵ_r	Dielectric constant	30

and spin distributions over the entire channel and under different conditions are in the Supplemental Material [17] (Figs. S1 and S2).

Interestingly, the spins are found to accumulate not only close to the laser injection but also much farther than expected from the spin relaxation length ($L_s = \sqrt{D_n \tau_s} = 0.51 \mu\text{m}$) along the edges, as highlighted by the dashed boxes in Fig. 1. This spin accumulation is unlikely to be caused by ISHE, because the sign of the spin density is independent of circular polarization, always \downarrow (\uparrow) at the top (bottom) edge. Instead, it can be understood by the SHE-induced spin current transverse to the electron diffusion current from the laser injection point to the contact. Nevertheless, SHE-induced spin density is much smaller than that directly injected by circular photoexcitation and is unlikely to substantially affect HDPC.

B. Photocurrent map

To compare with experimentally measurable quantities, we calculate the total current by integrating the current density over the channel cross section under both LCP and RCP. Then HDPC can be found from the difference in photocurrent created by LCP to RCP, i.e., $I_{\text{HDPC}} = I_{\uparrow} - I_{\downarrow}$, and the total photocurrent by $I_{\text{sum}} = I_{\uparrow} + I_{\downarrow}$. Both I_{HDPC} and I_{sum} are calculated at various laser positions to construct a map.

We first present the photocurrent cross sections along the channel width [Figs. 2(a) and 2(b)]. I_{sum} largely stays flat as the laser is scanned along the width, but drops at the edge where the laser spot is only partially on the material. In contrast to I_{sum} , I_{HDPC} is only large when the laser is close to the edge, as the laser in the middle of the channel fails to generate charge accumulation as shown in Fig. 1(c). I_{HDPC} flips sign when the laser moves from the top edge to the bottom edge as is expected from the chiral ISHE current. The decay length

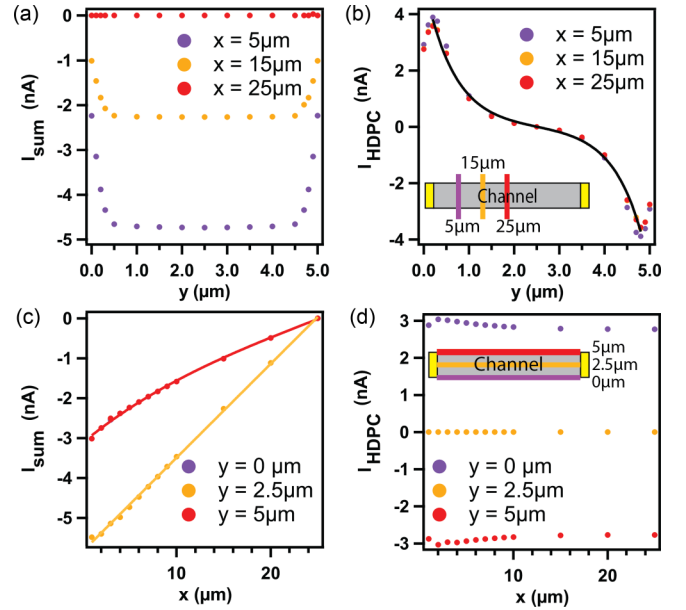


FIG. 2. The helicity-dependent (I_{HDPC}) and the total (I_{sum}) photocurrent as the laser is scanned along the channel width [(a), (b)] and length [(c), (d)] respectively. The insets in panels (b) and (d) show the paths of laser injection. Purple dots overlay perfectly with red in panel (c) and are difficult to see.

of I_{HDPC} extracted from Fig. 2(b) agrees well with L_s here and for a different L_s value (Fig. S3). This provides a convenient way to experimentally extract L_s from the spatially resolved HDPC.

Next, we examine the photocurrent cross sections along the channel length [Figs. 2(c) and 2(d)]. I_{sum} decays as the laser is scanned away from the contact, with decay lengths comparable to the minority carrier (hole) diffusion length (set to be $15 \mu\text{m}$). In contrast, I_{HDPC} is insensitive to the laser position as long as the laser moves along the channel edge, because the position of the battery (ISHE-induced local EMF) in a narrow channel does not change the steady-state current. It further indicates the ISHE-induced local EMF is independent of the laser position, which is reasonable as L_s is short ($0.51 \mu\text{m}$) and ISHE is locally unaffected by the contact.

The diffusion, drift, and ISHE current components can be found in Appendix C, which shows more details on understanding the current generation mechanisms. The dependence of HDPC on laser spot size, device dimensions, and SOI strength is also consistent with expectations shown in Appendix E.

C. Doping effects

We simulate HDPC at doping concentrations varying from 10^{15} to 10^{18} m^{-2} , and consider both n - and p -type channels. We also ensure that the contact resistance is at least two orders of magnitude smaller than the channel resistance, by adjusting the barrier height to achieve a flat band bending at the contact (band diagrams shown in Fig. S4). The simulated I_{HDPC} only increases by a factor of 2 as the doping concentration increases by three orders of magnitude [Fig. 3(a)] and is independent of the channel type. HDPC can be understood

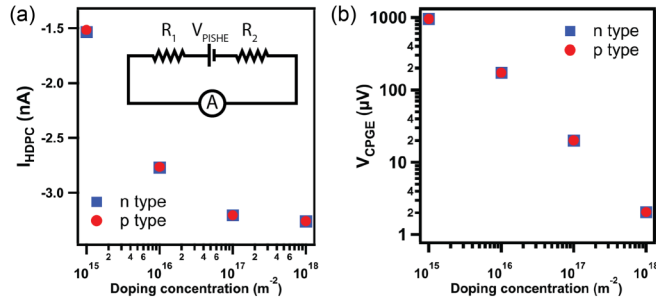


FIG. 3. Doping effects on HDPC. (a) I_{HDPC} , and (b) V_{PISHE} for both n (blue boxes) and p (red circles) type devices as a function of doping concentration. The inset in panel (a) is the equivalent circuit diagram of the device.

by an equivalent circuit model composed of a local helicity-dependent voltage source (V_{PISHE}) and a channel resistance ($R_{\text{total}} = R_1 + R_2$) as shown in Fig. 3(a) inset. The calculated $V_{\text{PISHE}} = I_{\text{HDPC}} R_{\text{total}}$ is consistent with the simulated potential difference in Fig. 1. Interestingly, V_{PISHE} is found to be inversely proportional to the doping concentration [Fig. 3(c)]. Previously, the weaker PISHE at a higher doping concentration was mainly attributed to the reduced τ_s [18]. However, τ_s is fixed in our simulation for all doping levels. So this strong doping dependence of V_{PISHE} is surprising.

We can understand this doping effect by considering the balance of the drift and diffusion currents near the laser injection point. When the laser is injected near the edge, ISHE-generated local electric field drives a drift current. The photoexcitation is close to the channel edge, where the total current flowing out of the edge must be zero. Therefore, the drift current must be canceled by the diffusion current near the photoexcitation to satisfy this boundary condition. The diffusion current is determined only by the Gaussian distribution of the local photoexcitation, independent of doping. Hence, the drift current must be independent of doping as well, but the drift current is determined by the product of majority carrier concentration (approximately equal to the doping concentration) and electric field. Consequently, the electric field and V_{PISHE} must be inversely proportional to the doping concentration. This intuitive understanding is supported by the simulation results, which show that photogenerated carrier concentration and the drift and diffusion currents remain largely unchanged when the doping concentration increases by orders of magnitude (Fig. S5). This result shows another mechanism that can significantly suppress PISHE at higher doping concentration, in addition to the τ_s reduction.

D. Band bending effects

Energy band bending often occurs at the semiconductor and metal junctions [19–22]. We now examine how this influences HDPC, by varying Φ_B from 0.03 to 0.25 eV, while fixing the doping at $N_d = 10^{16} \text{ m}^{-2}$. As Φ_B increases, $|I_{\text{sum}}|$ increases because of more efficient charge collection [Fig. 4(a)]. In contrast, $|I_{\text{HDPC}}|$ decreases when Φ_B increases [Figs. 4(b) and 4(c)]. This can be understood by the contact resistance increase. At fixed doping, both the channel resistance and V_{PISHE} (when laser is not too close to contact) are constant.

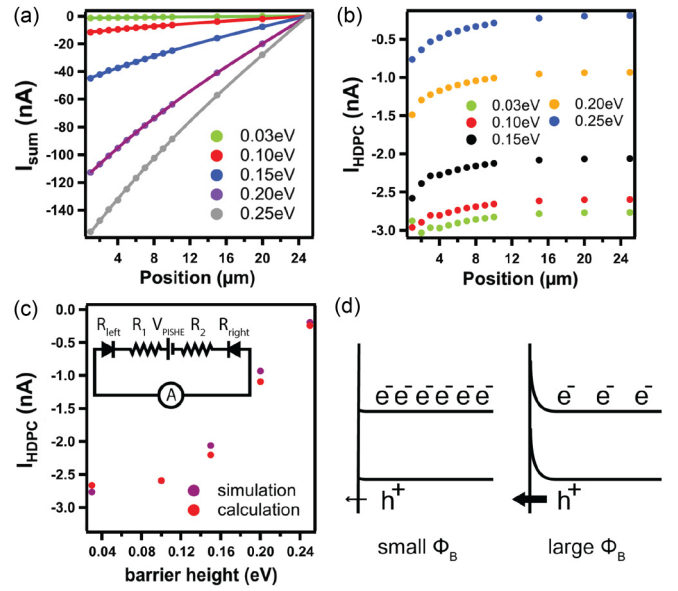


FIG. 4. Band bending effects on HDPC. (a) I_{sum} and (b) I_{HDPC} , as a function of laser position for various Φ_B values. (c) The simulated I_{HDPC} as a function of Φ_B , when the laser is injected at $(25, 5) \mu\text{m}$. The inset shows the equivalent circuit diagram of the device. I_{HDPC} calculated from the circular model, using $V_{\text{PISHE}} = 0.167 \text{ mV}$, agrees well with the simulation. (d) Band bending diagrams at different barrier heights. The larger band bending facilitates charge transfer and reduces electron concentration near the contact.

But the contact resistance increases as Φ_B increases, leading to reduced $|I_{\text{HDPC}}|$. As V_{PISHE} is small, the contact resistance can be found from the low bias limit of the diode: $R_{\text{contact}} = \frac{2k_B T}{qI_s}$, where the factor of 2 accounts for the two contacts. $I_s = WA_{2D} T^{3/2} \exp(-q\Phi_B/k_B T)$ is the saturation current, and $A_{2D} = q\sqrt{8\pi k_B^3 m_e/h^2}$ is the 2D Richardson constant for thermionic emission [23]. The calculated I_{HDPC} using the circuit model follows the simulated I_{HDPC} well [Fig. 4(c)].

The band bending also changes the HDPC distribution. $|I_{\text{HDPC}}|$ increases when the photoexcitation is close to the contact [Fig. 4(b)]. The large barrier height induces a larger increase in HDPC near the contact. We attribute the larger $|I_{\text{HDPC}}|$ near the contact to the increase of V_{PISHE} . Since the photogenerated carriers recombine rapidly at the metal contact, the carrier concentration drops when the laser is close to the contact. The reduction in carrier concentration leads to an increase of V_{PISHE} , as discussed in the previous section. As a larger contact band bending generates stronger charge flow to the contact, carrier concentration decreases more [Fig. 4(d)], leading to a larger increase of HDPC, consistent with the simulation results [Fig. 4(b)]. The HDPC increase near the contact is suppressed at a higher doping level (Fig. S6), because the photogeneration barely increases the total electron concentration in this case.

E. Spin relaxation effects

Like SOI strength, the values of τ_s also vary significantly over different materials. We now vary τ_s from 0.1 to 100 ns to study its effects on HDPC. $|I_{\text{HDPC}}|$ first increases linearly with

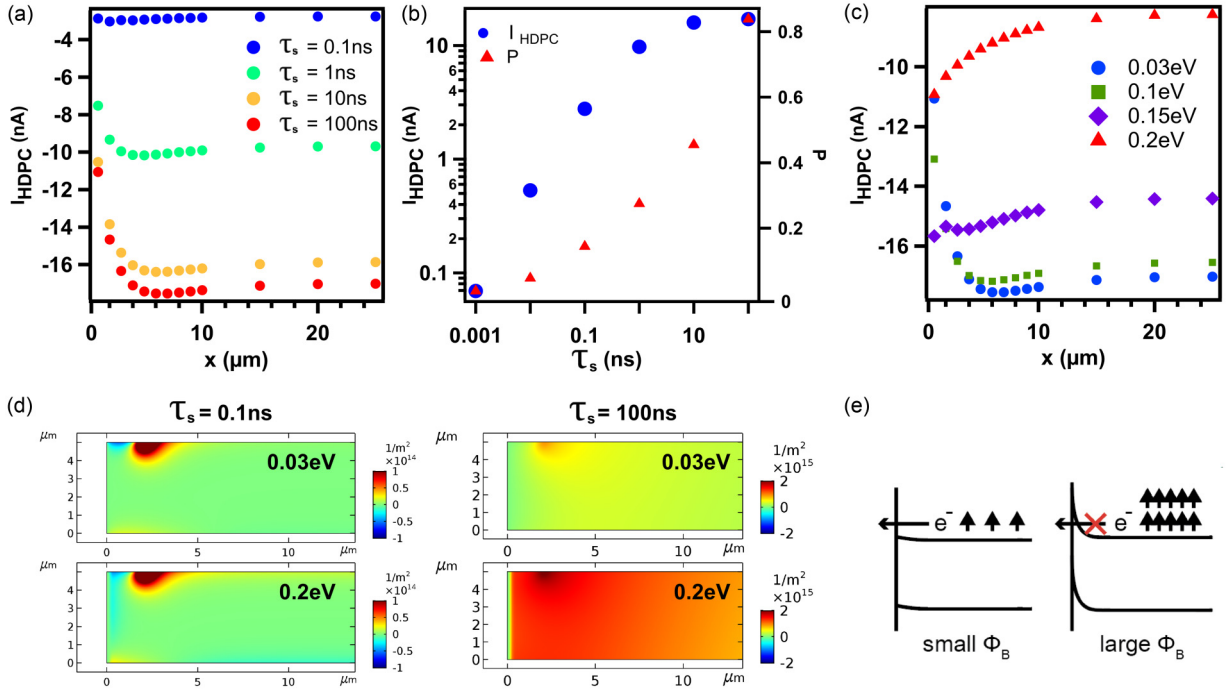


FIG. 5. Spin relaxation time-dependent HDPC distributions. (a) I_{HDPC} as a function of laser position at various τ_s . The laser is scanned along the top edge of the channel. Φ_B is fixed at 0.03 eV. (b) I_{HDPC} and the degree of spin polarization (P) at $(25, 5) \mu\text{m}$ as a function of τ_s . (c) I_{HDPC} as a function of laser position at various Φ_B and a fixed τ_s of 100 ns. (d) The spin density distributions at $\tau_s = 0.1$ and 100 ns, $\Phi_B = 0.03$ and 0.2 eV, respectively. The photoexcitation is fixed at $(2, 5) \mu\text{m}$. The doping concentration in all these simulations is fixed at 10^{16}m^{-2} . (e) A schematic diagram showing a higher spin density at large Φ_B , because electrons are blocked by the barrier.

τ_s , and then saturates when τ_s is longer than 10 ns [Fig. 5(b)]. The linear increase is expected since the spin density is proportional to $1/\tau_s$, as implied by Eq. (1) and confirmed by simulation (Fig. S7). The increase of spin density enhances the ISHE current and the dipolar charge accumulation, leading to a higher HDPC. But when τ_s is comparable to the carrier recombination lifetime (set to be 100 ns), the increase of I_{HDPC} begins to saturate, as the carrier recombination also decreases the spin density (Fig. S8). We have also calculated the degree of spin polarization of photogenerated carriers, $P = |s|/\Delta n$, where $s = n_{\uparrow} - n_{\downarrow}$ is the spin polarization density and Δn is the photoexcited electron density. P at the laser position increases from close to zero to near 100% as τ_s increases [Fig. 5(b)].

The I_{HDPC} distributions are also influenced by τ_s . When the laser is injected close to the contact, $|I_{\text{HDPC}}|$ drops [Fig. 5(a)] for longer τ_s . This can be understood by the fast spin relaxation at the contact. If the laser injection is within L_s to the contact, the contact acts as a fast spin relaxation pathway, which can effectively decrease the photo-induced spin density and HDPC.

Finally, we comment on the opposite trends observed in the HDPC distributions, where $|I_{\text{HDPC}}|$ increases near the contact in Fig. 4(b) but decreases in Fig. 5(a). This can be understood as there are two competing mechanisms that determine the HDPC behavior near the contact: (1) fast carrier recombination at the contact, which reduces the carrier density and leads to stronger HDPC, and (2) fast spin relaxation at the contact, which reduces the spin density and leads to weaker HDPC.

Whether HDPC increases or decreases near the contact is determined by a combination of factors including L_s , doping concentration, and Φ_B . Only when L_s is larger than the laser spot size can the fast contact spin relaxation result in a detectable HDPC decrease near the contact. A large Φ_B increases band bending, leading to a greater reduction of carrier concentration and a HDPC increase near the contact, provided the doping concentration is not too high. A large Φ_B also prevents electron spins from reaching the contact [Fig. 5(e)], so that spin density and HDPC may not decrease much near the contact, as confirmed by the simulation [Figs. 5(c) and 5(d)]. The simulated $|I_{\text{HDPC}}|$ decreases near the contact at small Φ_B , but gradually becomes flat and then increases as Φ_B increases [Fig. 5(c)], because contact carrier recombination becomes more important than contact spin relaxation. As discussed, the simulation shows that spatially resolved PISHE measurements may be used to extract spin relaxation length. A more reliable way to extract L_s is from the HDPC decay near the channel edge, since the HDPC behavior near the contact can be complex as shown.

IV. CONCLUSION

In conclusion, we have performed comprehensive COMSOL finite element simulations to model HDPC, with the consideration of the effects of device dimensions, SOI strength, doping, barrier height, and spin relaxation time. We summarize our main findings below: (1) The local spin injection near the edge of the channel results in a dipolar charge accumulation, which generates a circular polarization-dependent

EMF and photocurrent. (2) The ISHE-induced EMF is inversely proportional to the doping concentration because of the balance of the drift and diffusion currents near the photoexcitation. (3) HDPC remains largely unchanged when the laser is scanned along the channel edge, but when the laser is close to the contact, HDPC either increases or decreases depending on the simulation parameters. The fast contact charge recombination may result in HDPC increase near the contact, while the fast contact spin relaxation may decrease HDPC. (4) HDPC mapping may be used to extract the spin relaxation length of the channel material. The easiest way to do so is to extract L_s from the HDPC extension near the channel edge. The HDPC behavior near the contact is complicated and caution must be taken to interpret the data.

These simulations allow clear visualization of distributions of spin, charge, electric field, and drift, diffusion, and ISHE current densities. More important, our work provides a framework for the detailed understanding of PISHE under local photoexcitation and may help correctly interpret and extract useful information from the HDPC experimental results. The results also provide a clear physical picture to understand the doping effect on HDPC and offer guidance on optimizing spintronic materials for optical control of spin polarization.

See the Supplemental Material [17] for more details on the distributions of electric field; charge, spin, and current densities; I_{HDPC} mappings; energy band diagrams; and comparison of spin relaxation rates and carrier recombination rates. All files related to a published paper are stored as a single deposit.

ACKNOWLEDGMENTS

This work was supported by the U.S. National Science Foundation Grants No. DMR-1838532 and No. DMR-2105161.

APPENDIX A: BASIC EQUATIONS

First, electrons and holes satisfy the electrostatic equation,

$$\nabla \cdot \vec{E} = \frac{q(p + N_d - n - N_a)}{\epsilon_r \epsilon_0}, \quad (\text{A1})$$

where n (p) is the electron (hole) density, N_a (N_d) is the acceptor (donor) concentration, and ϵ_r is the dielectric constant. In our model, we assume that the hole spin relaxation is much faster than electrons, as electrons and holes are often asymmetric in realistic systems with distinct spin relaxation lifetimes. In this scenario, the hole spin polarization is assumed to be zero. If both electron and hole spins are considered and they have similar spin diffusion lengths, it is likely the ISHE currents for the electrons and holes will cancel each other. Future work is needed to confirm this speculation. Since the hole spin polarization is assumed to be zero, the continuity equation for holes becomes

$$\frac{dp}{dt} = G - b(np - n_i^2) - \nabla \cdot \vec{J}_p. \quad (\text{A2})$$

The Shockley-Read-Hall recombination occurs at a rate b ,

$$b = \frac{1}{\tau_p(n + n_i) + \tau_n(p + n_i)}, \quad (\text{A3})$$

where τ_n and τ_p are electron and hole recombination lifetime, respectively. J_p is the number hole current density given by

$$\vec{J}_p = \mu_p p \vec{E} - D_p \nabla p, \quad (\text{A4})$$

where μ_p is the hole mobility and $D_p = \mu_p k_B T / e$ is the hole diffusion coefficient.

Summing Eq. (1) for both spins yields the continuity equation for all electrons:

$$\frac{dn}{dt} = G - b(np - n_i^2) - \nabla \cdot \vec{J}_n. \quad (\text{A5})$$

The total electron current density can be found by the addition of the \uparrow and \downarrow currents in Eq. (2):

$$\vec{J}_n = -\mu_n n \vec{E} - D_n \nabla n + \vec{J}_n^{\text{ISHE}}, \quad (\text{A6})$$

$$\vec{J}_n^{\text{ISHE}} = \gamma \mu_n \vec{E} \times \vec{s} + \gamma D_n \nabla \times \vec{s}, \quad (\text{A7})$$

where $\vec{s} = s \hat{z} = (n_\uparrow - n_\downarrow) \hat{z}$ is the spin polarization density vector. This result is consistent with Eq. (5) in Ref. [24].

APPENDIX B: SIMULATION DETAILS

The focused laser beam follows a Gaussian profile, with a carrier generation rate of $G = G_0 \exp\{-[(x - x_0)^2 + (y - y_0)^2]/(2\sigma^2)\}$. A finite element mesh size as small as 5 nm is used in regions where carrier densities vary rapidly near contact and laser injection. The simulations generate distributions of charge and spin densities, as well as drift, diffusion, and ISHE-induced current densities.

We make the following assumptions in the simulation. (1) The hole spins relax much more quickly than electron spins. (2) We use medium laser intensity so that $n \approx n_0$ and $p \gg p_0$, where n_0 and p_0 are electron and hole concentrations in the dark, respectively. (3) We consider 2D effective density of states (DOS), as HDPC is often studied in quantum wells or in the surface states of TIs. So we have $N_C = \frac{g_c m_e k_B T}{\pi \hbar^2}$ and $N_V = \frac{g_v m_h k_B T}{\pi \hbar^2}$, where N_C is the effective DOS at the conduction band edge, g_c is the degeneracy, and m_e is the electron effective mass. N_V , g_v , and m_h are their counterparts for the valence band and holes. (4) At the metal contacts, the recombination and spin relaxation are infinitely fast and hence $n = n_0$, $p = p_0$, $n_\uparrow = n_\downarrow$ at $x = 0, L$. (5) The device reaches a steady state where all physical quantities are time independent. (6) We ignore the photothermoelectric effect.

The 2D COMSOL simulation has certain limitations which we summarize below. (1) The 2D Poisson's equation [Eq. (A1)] is considered and the out-of-plane and out-of-edge electric field is ignored. This may lead to an overestimation of the electric field in the device channel. (2) We treat the material as a semiconductor with a bandgap of 0.3 eV and nonzero electron and hole effective mass, though the surface states of TIs have a linear dispersion relation with vanishing electron effective mass. These limitations may lead to the deviation of quantitative predictions of the model from the realistic measurements, but the general conclusions are expected to be robust against these details.

APPENDIX C: CURRENT COMPONENTS

We plot all eight current components in Fig. 6, including hole diffusion and drift, spin-polarized electron diffusion and drift, and their corresponding ISHE components. The

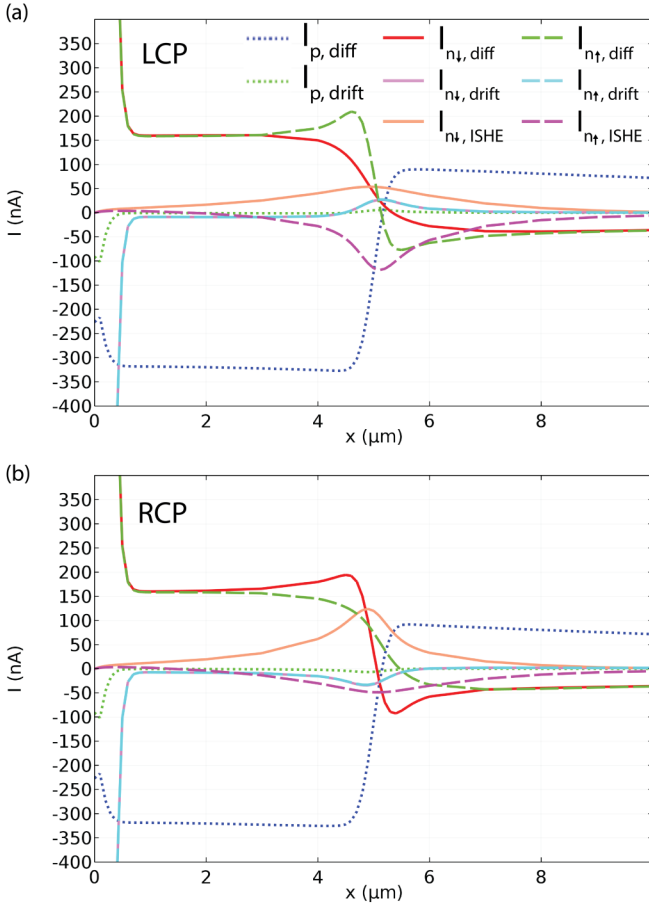


FIG. 6. Distributions of current components induced by the laser injected at $(5, 5) \mu\text{m}$ with LCP (a) and RCP (b). Current flux of each component is calculated by integrating its corresponding current density over the y cross section perpendicular to the channel.

complete distributions over the entire channel are in the Supplemental Material [17] (Fig. S9). We highlight a few key observations below: (1) The current components become very large near the contact, because of the large electric field in the depletion region. (2) The diffusion current is much larger than the drift current outside the depletion region, because the induced dipole creates a rather weak electric field. (3) Under LCP, the diffusion current and the ISHE current of \uparrow electrons are larger than those of \downarrow . This trend is reversed for RCP, clearly indicating HDPC. (4) The ISHE current is only large close to the laser position with a decay length similar to L_s . Though the ISHE current is local, it can still produce HDPC, because the ISHE-induced EMF can drive a spin-dependent current through the device channel. (5) The $I_{n\uparrow, \text{diff}}$ under LCP and $I_{n\downarrow, \text{diff}}$ under RCP have slightly different shapes. For example, the bump of the dashed green curve in Fig. 6(a) is slightly more pronounced than that of the solid red curve in Fig. 6(b). This appears to be bizarre at first glance, as we expect flipping the circular polarization would simply change spin up to spin down while keeping the shape of current distribution the same. We attribute the symmetry breaking to the contact proximity effect. The laser here is injected near the left contact. The injected carriers diffuse to the contact, leading to a charge current (Fig. S1). As a result

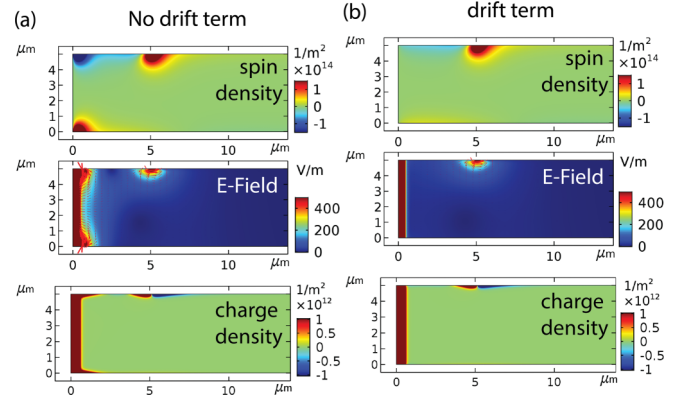


FIG. 7. Spin, electric field, and charge distributions for simulation without (a) and with (b) considering drift-induced ISHE current, respectively. The distributions of the spin, electric field, and charge in the whole channel are shown in Figs. S10(a) and S10(b).

of SHE, opposite spins accumulate near the top and bottom edges. Interestingly, the sign of the spin accumulation is independent of circular polarization as shown in Fig. S1. This is because the charge current direction is independent of circular polarization. The polarization-independent spin accumulation may affect the details of the current distributions and cause the observed asymmetry.

APPENDIX D: DRIFT EFFECTS ON ISHE CURRENT

Both the drift and diffusion terms in Eq. (3) can create a transverse charge current by ISHE. However, the drift term was not considered in previous work [2,4,6] without rigorous justification. Our simulation work provides an opportunity to scrutinize its validity. Ignoring the drift term results in strong electric field and spin-charge accumulation near the corners of the contact [Fig. 7(a)]. The simulation produces no such

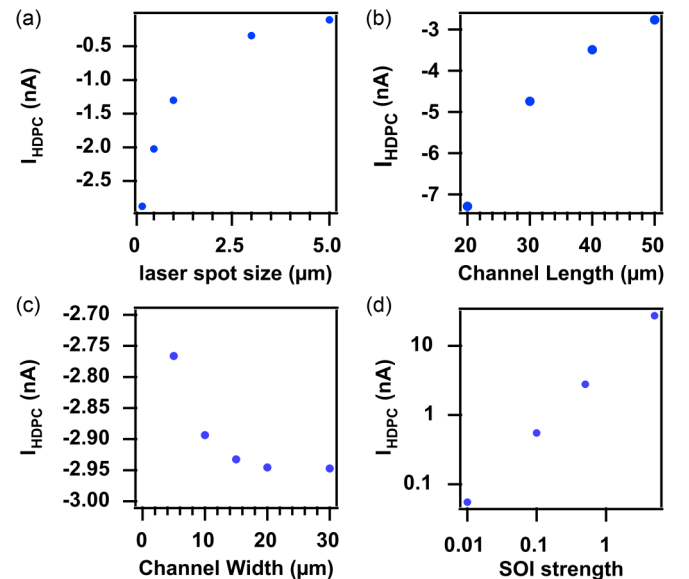


FIG. 8. I_{HDPC} as a function of (a) laser spot size, (b) channel length, (c) width, and (d) SOI strength. The laser is centered at $(25, 5) \mu\text{m}$.

results when the drift terms are considered [Fig. 7(b)]. As both the diffusion and drift current components in the depletion region are strong, a large transverse spin current is created if the drift term is not considered in the ISHE current density. The spin and charge accumulation still occurs even without photoexcitation as shown in Fig. S10(c), as the large drift current in the depletion region does not require photoexcitation. Though ignoring the drift term clearly causes false prediction of charge buildup near the contact, its effect on the overall HDPC is small under our simulation parameters. This is likely because the diffusion current component is much larger than the drift component over most parts of the channel (Fig. 6).

APPENDIX E: DEPENDENCE ON LASER SPOT SIZE, DEVICE DIMENSIONS, AND SOI STRENGTH

We have also investigated the I_{HDPC} dependence on the laser spot size, the device dimensions, and the SOI strength.

$|I_{\text{HDPC}}|$ decreases as the laser spot size increases [Fig. 8(a)], since the spin density gradient is reduced, resulting in a weaker ISHE-induced EMF. $|I_{\text{HDPC}}|$ decreases as the channel length increases [Fig. 8(b)] because the channel resistance increases. $|I_{\text{HDPC}}|$ only increases by 7% as the channel width increases by six times [Fig. 8(c)]. Even though the overall channel resistance decreases significantly in the wider channel device, the ISHE-induced local electric dipole at the top edge mainly drives a current near the top part of the channel. The current density at the lower part is small and does not contribute much to the total current. The values of SOI strength, which can be experimentally measured by the spin Hall angle, vary in a large range in different materials, ranging from $\gamma = 10^{-3}$ to 10 [1,25–27]. The simulated I_{HDPC} is linear with γ [Fig. 8(d)]. This is expected since J_n^{ISHE} is proportional to γ in Eq. (3). As γ increases, charge accumulates more near the edge, leading to stronger electric field and HDPC.

-
- [1] J. Sinova, S. O. Valenzuela, J. Wunderlich, C. H. Back, and T. Jungwirth, Spin Hall effects, *Rev. Mod. Phys.* **87**, 1213 (2015).
- [2] X. W. He, B. Shen, Y. Chen, Q. Zhang, K. Han, C. M. Yin, N. Tang, F. J. Xu, C. G. Tang, Z. J. Yang, Z. X. Qin, G. Y. Zhang, and Z. G. Wang, Anomalous Photogalvanic Effect of Circularly Polarized Light Incident on the Two-Dimensional Electron Gas in $\text{Al}_x\text{Ga}_{1-x}\text{N}/\text{GaN}$ Heterostructures at Room Temperature, *Phys. Rev. Lett.* **101**, 147402 (2008).
- [3] F. Mei, N. Tang, X. Wang, J. Duan, S. Zhang, Y. Chen, W. Ge, and B. Shen, Detection of spin-orbit coupling of surface electron layer via reciprocal spin Hall effect in InN films, *Appl. Phys. Lett.* **101**, 132404 (2012).
- [4] J. Yu, X. Zeng, L. Zhang, K. He, S. Cheng, Y. Lai, W. Huang, Y. Chen, C. Yin, and Q. Xue, Photoinduced inverse spin Hall effect of surface states in the topological insulator Bi_2Se_3 , *Nano Lett.* **17**, 7878 (2017).
- [5] D.-X. Qu, X. Che, X. Kou, L. Pan, J. Crowhurst, M. R. Armstrong, J. Dubois, K. L. Wang, and G. F. Chapline, Anomalous helicity-dependent photocurrent in the topological insulator $(\text{Bi}_{0.5}\text{Sb}_{0.5})_2\text{Te}_3$ on a GaAs substrate, *Phys. Rev. B* **97**, 045308 (2018).
- [6] D. Fan, R. Hobarra, R. Akiyama, and S. Hasegawa, Inverse spin Hall effect induced by asymmetric illumination of light in topological insulator Bi_2Se_3 , *Phys. Rev. Research* **2**, 023055 (2020).
- [7] C. L. Yang, H. T. He, L. Ding, L. J. Cui, Y. P. Zeng, J. N. Wang, and W. K. Ge, Spectral Dependence of Spin Photocurrent and Current-Induced Spin Polarization in an InGaAs/InAlAs Two-Dimensional Electron Gas, *Phys. Rev. Lett.* **96**, 186605 (2006).
- [8] S. D. Ganichev, E. L. Ivchenko, S. N. Danilov, J. Eroms, W. Wegscheider, D. Weiss, and W. Prettl, Conversion of Spin Into Directed Electric Current in Quantum Wells, *Phys. Rev. Lett.* **86**, 4358 (2001).
- [9] J. McIver, D. Hsieh, H. Steinberg, P. Jarillo-Herrero, and N. Gedik, Control over topological insulator photocurrents with light polarization, *Nat. Nanotechnol.* **7**, 96 (2012).
- [10] D. Fu, J. Zou, K. Wang, R. Zhang, D. Yu, and J. Wu, Electrothermal dynamics of semiconductor nanowires under local carrier modulation, *Nano Lett.* **11**, 3809 (2011).
- [11] R. Graham and D. Yu, Scanning photocurrent microscopy in semiconductor nanostructures, *Mod. Phys. Lett. B* **27**, 1330018 (2013).
- [12] C. Zucchetti, F. Bottegoni, C. Vergnaud, F. Ciccacci, G. Isella, L. Ghirardini, M. Celebrano, F. Rortais, A. Ferrari, A. Marty, M. Finazzi, and M. Jamet, Imaging spin diffusion in germanium at room temperature, *Phys. Rev. B* **96**, 014403 (2017).
- [13] S. Dhara, E. J. Mele, and R. Agarwal, Voltage-tunable circular photogalvanic effect in silicon nanowires, *Science* **349**, 726 (2015).
- [14] Y. Pan, Q.-Z. Wang, A. L. Yeats, T. Pillsbury, T. C. Flanagan, A. Richardella, H. Zhang, D. D. Awschalom, C.-X. Liu, and N. Samarth, Helicity dependent photocurrent in electrically gated $(\text{Bi}_{1-x}\text{Sb}_x)_2\text{Te}_3$ thin films, *Nat. Commun.* **8**, 1037 (2017).
- [15] I. Žutić, J. Fabian, and S. Das Sarma, Spin injection through the depletion layer: A theory of spin-polarized pn junctions and solar cells, *Phys. Rev. B* **64**, 121201(R) (2001).
- [16] Y. Hou, R. Wang, R. Xiao, L. McClintock, H. C. Travaglini, J. P. Francia, H. Fetsch, O. Erten, S. Y. Savrasov, B. Wang *et al.*, Millimetre-long transport of photogenerated carriers in topological insulators, *Nat. Commun.* **10**, 5723 (2019).
- [17] See Supplemental Material at <http://link.aps.org/supplemental/10.1103/PhysRevB.104.205413> for more information about the our simulation work.
- [18] J. Wu, H. M. Hao, Y. Liu, Y. Zhang, X. L. Zeng, S. B. Zhu, Z. C. Niu, H. Q. Ni, and Y. H. Chen, Anomalous circular photogalvanic effect in p-GaAs, *Opt. Express* **29**, 13829 (2021).
- [19] C. Ojeda-Aristizabal, M. Fuhrer, N. P. Butch, J. Paglione, and I. Appelbaum, Towards spin injection from silicon into topological insulators: Schottky barrier between Si and Bi_2Se_3 , *Appl. Phys. Lett.* **101**, 023102 (2012).
- [20] A. Hussain and A. Rahman, Electrical and photovoltaic characteristics of Ni/(n) Bi_2S_3 Schottky barrier junction, *Superlattices Microstruct.* **80**, 39 (2015).
- [21] T. U. Kampen and W. Mönch, Barrier heights of GaN Schottky contacts, *Appl. Surf. Sci.* **117**, 388 (1997).
- [22] Z. Lin, W. Lu, J. Lee, D. Liu, J. S. Flynn, and G. R. Brandes, Barrier heights of Schottky contacts on strained AlGaIn/GaN

- heterostructures: Determination and effect of metal work functions, *Appl. Phys. Lett.* **82**, 4364 (2003).
- [23] A. Anwar, B. Nabet, J. Culp, and F. Castro, Effects of electron confinement on thermionic emission current in a modulation doped heterostructure, *J. Appl. Phys.* **85**, 2663 (1999).
- [24] M. I. Dyakonov, Spin Hall effect, *Int. J. Mod. Phys. B* **23**, 2556 (2009).
- [25] Z. S. Popović, J. M. Kurdestany, and S. Satpathy, Electronic structure and anisotropic Rashba spin-orbit coupling in monolayer black phosphorus, *Phys. Rev. B* **92**, 035135 (2015).
- [26] N. H. D. Khang, Y. Ueda, and P. N. Hai, A conductive topological insulator with large spin Hall effect for ultralow power spin-orbit torque switching, *Nat. Mater.* **17**, 808 (2018).
- [27] Y. Fan, P. Upadhyaya, X. Kou, M. Lang, S. Takei, Z. Wang, J. Tang, L. He, L.-T. Chang, M. Montazeri *et al.*, Magnetization switching through giant spin-orbit torque in a magnetically doped topological insulator heterostructure, *Nat. Mater.* **13**, 699 (2014).